Int J Fract (2013) 184:137–149
DOI 10.1007/s10704-013-9846-z

Statistics of ductile fracture surfaces: the effect of material parameters

Laurent Ponson · Yuanyuan Cao · Elisabeth Bouchaud · Viggo Tvergaard · Alan Needleman

Received: 21 January 2013 / Accepted: 26 March 2013 / Published online: 9 April 2013

Abstract The effect of material parameters on the statistics of fracture surfaces is analyzed under small scale yielding conditions. Three dimensional calculations of ductile crack growth under mode I plane strain, small scale yielding conditions are carried out using an elastic-viscoplastic constitutive relation for a progressively cavitating plastic solid with two populations of void nucleating second phase particles represented. Large particles that result in void nucleation at an early stage are modeled discretely while small particles that require large strains to nucleate are homogeneously distributed. The three dimensional analysis permits modeling of a three dimensional material microstructure and of the resulting three dimensional stress and deformation states that develop in the fracture process region. Material parameters characterizing void nucleation are varied and the statistics of the resulting fracture surfaces is investigated. All the fracture surfaces are found to be self-affine over a size range of about two orders of magnitude with a very similar roughness exponent of 0.56 ± 0.03. In contrast, the full statistics of the fracture surfaces is found to be more sensitive to the material microscopic fracture properties: height fluctuations are shown to crossover from a Student's distribution with power law tails at small scales to a Gaussian behavior at large scales, but this transition occurs at a material dependent length scale. Using the family of Student's distributions, this transition can be described introducing an additional exponent $\mu = 0.15 \pm 0.02$, the value of which compares well with recent experimental findings. The description of the roughness distribution used here gives a more complete quantitative characterization of the fracture surface morphology which allows a better comparison with experimental data and an easier interpretation of the roughness properties in terms of microscopic failure mechanisms.

Keywords Fracture surfaces · Roughness statistics · Ductile fracture · Crack growth · Scaling behavior · Finite elements

L. Ponson · Y. Cao
Institut Jean le Rond d'Alembert (UMR 7190), CNRS, Université Pierre et Marie Curie, Paris, France

E. Bouchaud
CEA-Saclay and ESPCI, Paris Tech, Paris, France

V. Tvergaard
Department of Mechanical Engineering, The Technical University of Denmark, Lyngby, Denmark

A. Needleman (✉)
Department of Materials Science and Engineering, University of North Texas, Denton, TX, USA
e-mail:needle@unt.edu

1 Introduction

Mandelbrot et al. (1984) first characterized the self-affine scaling properties of fracture surfaces. A hope in this study was to provide a quantitative correlation between fracture surface roughness and a material's crack growth resistance. This hope has yet to be

realized. Nevertheless, Mandelbrot et al. (1984) stimulated a large body of experimental and theoretical work aimed at characterizing the scaling properties of fracture surfaces. Experimentally, the self-affine nature of the roughness of fracture surfaces has been observed in a wide variety of materials (metals, ceramics, glasses, rocks…) under a wide variety of loading conditions (quasi-static, dynamic, fatigue) and is typically characterized by two exponents: one measured parallel to the crack front, denoted by ζ, and one measured along the crack propagation direction, denoted by β, see Ponson (2007), Alava et al. (2006), Bonamy and Bouchaud (2011) for overviews. In some studies, e.g. Bouchaud et al. (1990), Måløy et al. (1992), it was suggested that the values of these exponents are universal.

Others have maintained that the characterization of the roughness of fracture surfaces is more complex. For example, in Bonamy and Bouchaud (2011), Bonamy et al. (2006) it is argued that there are two roughness regimes: one pertaining to length scales smaller than the fracture process zone and the other to length scales larger than the fracture process zone, with each regime characterized by different values of the fracture surface roughness exponents. Alternatively, a multifractal characterization of fracture surface roughness has been suggested as discussed in Cherepanov et al. (1995). The extent to which the appropriate characterization of fracture surface roughness depends on the material microstructure and/or the fracture mechanism remains an open question.

A variety of theoretical analyses of fracture surface roughness have been carried out using a linear elastic fracture mechanics framework, e.g. Ramanathan et al. 1997, or a molecular dynamics framework, e.g. Nakano et al. (1995). For ductile fracture of structural metals at room temperature the governing mechanism is the nucleation, growth and coalescence of micron scale voids, which involves large plastic deformations, and occurs over size and time scales much larger than currently accessible by molecular dynamics. This process governs the evolution of ductile fracture surface roughness. The importance of accounting for porosity evolution and the accompanying plastic deformation in modeling fracture surface roughness is emphasized in Bouchaud (2003), Bouchbinder et al. (2004).

Calculations of fracture surface roughness using a finite deformation continuum mechanics formulation for a progressively cavitating solid were carried out in Needleman et al. (2012). The analyses in Needleman et al. (2012) were based on a modified Gurson (1975) constitutive relation for a porous viscoplastic solid with two types of void nucleating particles modeled: large particles that nucleate voids at an early stage and smaller particles that nucleate voids at a later stage. The larger particles were represented as uniform sized discrete "islands" of void nucleation, thus introducing a material length scale, while the smaller particles were uniformly distributed. This framework naturally accounts for the effects of damage evolution on the stress and deformation state in the fracture process zone.

In Needleman et al. (2012), the calculations were carried out for fixed material properties but for four random distributions of the larger particles. Here, we employ the same theoretical framework as in Needleman et al. (2012) and solve the same small scale yielding problem. We focus attention on one of the four spatial distributions of the larger particles in Needleman et al. (2012) and vary two material parameters that characterize void nucleation. We also use a more robust procedure to define the fracture surface geometry from the output of our simulations and investigate the roughness statistical properties for the cases calculated in Needleman et al. (2012) as well as for the simulations presented here. We go beyond the characterization of fracture surfaces by their correlation function and the value of the roughness exponent, and investigate the scaling of the full distribution of roughness. This scaling can be described by a second exponent characterizing the transition from power law tail at small scales to Gaussian roughness statistics at large scales. This quantitative characterization of fracture surface geometry allows a better comparison with experimental data and an easier interpretation of the roughness properties in terms of microscopic failure mechanisms.

2 Problem formulation

The boundary value problem analyzed is identical to that in Needleman et al. (2012). Only parameters characterizing void nucleation differ. For completeness, the formulation and constitutive relation are briefly stated here.

The focus is on quasi-static crack growth but dynamic analyses are carried out for numerical reasons. The calculations are carried out using a Lagrangian, convected coordinate formulation and the dynamic

principle of virtual work written as

$$\int_V \tau^{ij}\delta E_{ij}\,dV = \int_S T^i \delta u_i\,dS - \int_V \rho\frac{\partial^2 u^i}{\partial t^2}\delta u_i\,dV \quad (1)$$

All field quantities are taken to be functions of the convected coordinates, y^i, and time, t; E_{ij} are the covariant components of the Lagrangian strain tensor, T^i are the contravariant components of the traction vector, τ^{ij} are the contravariant components of Kirchhoff stress on the deformed convected coordinate net ($\boldsymbol{\tau} = J\boldsymbol{\sigma}$, with $\boldsymbol{\sigma}$ being the Cauchy or true stress and J the ratio of current to reference volume), v_j and u_j are the covariant components of the reference surface normal and displacement vectors, respectively, ρ is the mass density, V and S are the volume and surface of the body in the reference configuration, and $(\,)_{,i}$ denotes covariant differentiation in the reference (y^1, y^2, y^3) Cartesian frame. In presenting the results we will use the notations x, y and z for y^1, y^2 and y^3, respectively.

A slice of material orthogonal to the initial crack plane is analyzed and the quasi-static mode I isotropic elastic singular displacement field is imposed on the remote boundaries. Also imposed are symmetry conditions corresponding to an overall plane strain constraint.

As in Needleman et al. (2012), the in-plane block dimensions are $h_x = h_y = 0.4\,\text{m}$ with an initial crack tip with an opening of $b_0 = 1.875 \times 10^{-4}\,\text{m}$. The finite element mesh consists of 428, 256 twenty node brick elements giving 1, 868, 230 nodes and 5, 604, 690 degrees of freedom. Ten uniformly spaced elements are used through the thickness h_z of 0.005 m, with 10 elements through the thickness, and a uniform 208×64 in-plane mesh is used in a $0.02\,\text{m} \times 0.006\,\text{m}$ region immediately in front of the initial crack tip giving an in-plane element size of $9.62 \times 10^{-5}\,\text{m}$ by $9.38 \times 10^{-5}\,\text{m}$.

2.1 Constitutive relation

The constitutive framework is the modified Gurson constitutive relation with

$$\mathbf{d} = \mathbf{d}^e + \mathbf{d}^\Theta + \mathbf{d}^p \quad (2)$$

and

$$\mathbf{d}^e = \mathbf{L}^{-1} : \hat{\boldsymbol{\sigma}} \quad (3)$$

$$\mathbf{d}^\Theta = \alpha\dot{\Theta}\mathbf{I} \quad (4)$$

$$\mathbf{d}^p = \left[\frac{(1-f)\bar{\sigma}\dot{\bar{\epsilon}}}{\boldsymbol{\sigma} : \frac{\partial\Phi}{\partial\boldsymbol{\sigma}}}\right]\frac{\partial\Phi}{\partial\boldsymbol{\sigma}} \quad (5)$$

Small elastic strains are assumed, $\mathbf{L}$ is the tensor of isotropic elastic moduli, $\hat{\boldsymbol{\sigma}}$ is the Jaumann rate of Cauchy stress and Θ is the temperature.

Adiabatic conditions are assumed so that

$$\rho c_p\frac{\partial\Theta}{\partial t} = \chi\boldsymbol{\tau} : \mathbf{d}^p \quad (6)$$

with $\rho = 7,600\,\text{kg/m}^3 = 7.6 \times 10^{-3}\,\text{MPa/(m/sec)}^2$, $c_p = 465\,\text{J/(kg°K)}$, $\chi = 0.9$ and α in Eq. (4) is 1×10^{-5}/K.

The flow potential is (Gurson 1975),

$$\Phi = \frac{\sigma_e^2}{\bar{\sigma}^2} + 2q_1 f^* \cosh\left(\frac{3q_2\sigma_h}{2\bar{\sigma}}\right) - 1 - \left(q_1 f^*\right)^2 = 0 \quad (7)$$

where $q_1 = 1.25$, $q_2 = 1.0$ are parameters introduced in Tvergaard (1981), Tvergaard (1982a), f is the void volume fraction, $\bar{\sigma}$ is the matrix flow strength, and

$$\sigma_e^2 = \frac{3}{2}\boldsymbol{\sigma}' : \boldsymbol{\sigma}', \quad \sigma_h = \frac{1}{3}\boldsymbol{\sigma} : \mathbf{I}, \quad \boldsymbol{\sigma}' = \boldsymbol{\sigma} - \sigma_h\mathbf{I} \quad (8)$$

The function f^*, introduced in Tvergaard and Needleman (1984), is given by

$$f^* = \begin{cases} f & f < f_c \\ f_c + (1/q_1 - f_c)(f - f_c)/(f_f - f_c) & f \geq f \end{cases} \quad (9)$$

where the values $f_c = 0.12$ and $f_f = 0.25$ are used.

The matrix plastic strain rate, $\dot{\bar{\epsilon}}$, is taken as

$$\dot{\bar{\epsilon}} = \dot{\epsilon}_0\left[\frac{\bar{\sigma}}{g(\bar{\epsilon}, \Theta)}\right]^{1/m},$$
$$g(\bar{\epsilon}, \Theta) = \sigma_0 G(\Theta)\left[1 + \bar{\epsilon}/\epsilon_0\right]^N \quad (10)$$

with $\bar{\epsilon} = \int \dot{\bar{\epsilon}}dt$, $E = 70$ GPa, $\nu = 0.3$, $\sigma_0 = 300$ MPa ($\epsilon_0 = \sigma_0/E = 0.00429$), $N = 0.1$, $m = 0.01$ and $\dot{\epsilon}_0 = 10^3$/s.

The function defining the temperature-dependence of the flow strength is

$$G(\Theta) = 1 + b_G\exp(-c[\Theta_0 - 273]) \times \left[\exp(-c[\Theta - \Theta_0]) - 1\right] \quad (11)$$

with $b_G = 0.1406$ and $c = 0.00793$/K. In (11), Θ and Θ_0 are in K and $\Theta_0 = 293$K. Also, the initial temperature is taken to be uniform and 293K.

The initial void volume fraction is taken to be zero and the evolution of the void volume fraction is governed by

$$\dot{f} = (1 - f)\mathbf{d}^p : \mathbf{I} + \dot{f}_{nucl} \tag{12}$$

where the first term on the right hand side of Eq. (12) accounts for void growth and the second term for void nucleation.

Eight point Gaussian integration is used in each twenty node element for integrating the internal force contributions. Lumped masses are used and twenty-seven point Gaussian integration is used for the element mass matrix. The discretized equations are integrated using the explicit Newmark β-method ($\beta = 0$), Belytschko et al. (1976). The constitutive updating is based on the rate tangent modulus method of Peirce et al. (1984) while material failure is implemented via the element vanish technique in Tvergaard (1982b).

2.2 Inclusions and fracture properties

The calculations model a material with two populations of void nucleating second phase particles: (1) uniformly distributed small particles that are modeled by plastic strain controlled nucleation and (2) large, low strength inclusions that are modeled as "islands" of stress controlled nucleation. In each case, void nucleation is assumed to be described by a normal distribution as in Chu and Needleman (1980).

For plastic strain nucleation,

$$\dot{f}_{nucl} = D\dot{\bar{\epsilon}}, \quad D = \frac{f_N}{s_N\sqrt{2\pi}} \exp\left[-\frac{1}{2}\left(\frac{\bar{\epsilon} - \epsilon_N}{s_N}\right)^2\right] \tag{13}$$

The parameters $f_N = 0.04$ and $s_N = 0.1$ are fixed.

For stress controlled nucleation

$$\dot{f}_{nucl} = A\left[\dot{\bar{\sigma}} + \dot{\sigma}_h\right] \tag{14}$$

with

$$A = \frac{f_N}{s_N\sqrt{2\pi}} \exp\left[-\frac{1}{2}\left(\frac{\bar{\sigma} + \sigma_h - \sigma_N}{s_N}\right)^2\right] \tag{15}$$

if $(\bar{\sigma} + \sigma_h)$ is at its maximum over the deformation history. Otherwise $A = 0$.

We confine attention to a single inclusion distribution that is the distribution labeled 411 in Needleman et al. (2012). There are 2016 possible inclusions (mean spacing about 6.7×10^{-4} m) in the uniform mesh region. Each inclusion radius is $r_0 = 1.5 \times 10^{-4}$ m. For an inclusion governed by stress nucleation centered at (y_0^1, y_0^2, y_0^3), the value of f_N in Eq. (15) at the point (y^1, y^2, y^3) is

$$f_N = \begin{cases} \bar{f}_N & \text{for } \sqrt{(y^1 - y_0^1)^2 + (y^2 - y_0^2)^2 + (y^3 - y_0^3)^2} \le r_0; \\ 0 & \text{for } \sqrt{(y^1 - y_0^1)^2 + (y^2 - y_0^2)^2 + (y^3 - y_0^3)^2} > r_0 \end{cases} \tag{16}$$

The values $\bar{f}_N = 0.04$ and $s_N/\sigma_0 = 0.2$ are fixed.

In the following, materials having various values of parameters characterizing void nucleation are investigated (Fig. 1). For all materials analyzed the inclusion distribution is that termed case411 in Needleman et al. (2012):

- Material # 1 has the parameter values analyzed in Needleman et al. (2012) which are $\epsilon_N = 0.3$ and $\sigma_N/\sigma_0 = 1.5$. The fracture surfaces for this case are calculated using the procedure introduced here for defining the roughness geometry and the statistical geometry of this case is investigated in more detail than in Needleman et al. (2012).
- Material # 2 has the nucleation strain of the small particles changed from the reference value to $\epsilon_N = 0.4$ with the nucleation stress of the inclusions fixed at $\sigma_N/\sigma_0 = 1.5$.
- Material #2x has the nucleation strain of the small particles changed from the reference value to $\epsilon_N = 0.2$ with the nucleation stress of the inclusions fixed at $\sigma_N/\sigma_0 = 1.5$. This calculation terminated after an amount of crack growth that was too small to provide a fracture surface that could be characterized statistically in the same manner as for the other cases.
- Material # 3 has the nucleation stress of the inclusions changed from the reference value to $\sigma_N/\sigma_0 = 2.0$ with the nucleation strain of the small particles fixed at $\epsilon_N = 0.3$.

The results of the calculations are regarded as modeling quasi-static response via dynamic relaxation. The results are reported as for a quasi-static solution; for example, the absolute magnitude of geometric dimensions do not matter; only geometric ratios matter. In the following, the results are presented as for a quasi-static solution.

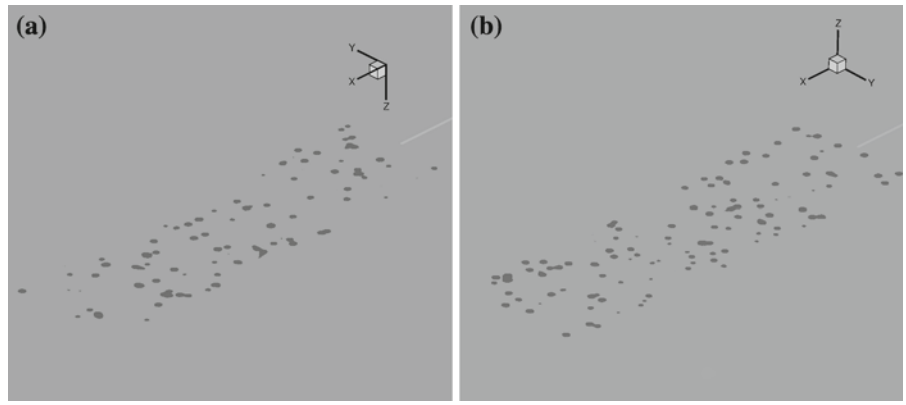

Fig. 1 Initial inclusion distribution. **a** On $z = 0$. **b** On $z = h_z$. Note that the positive $y-$axis is in opposite directions in **a** and **b**

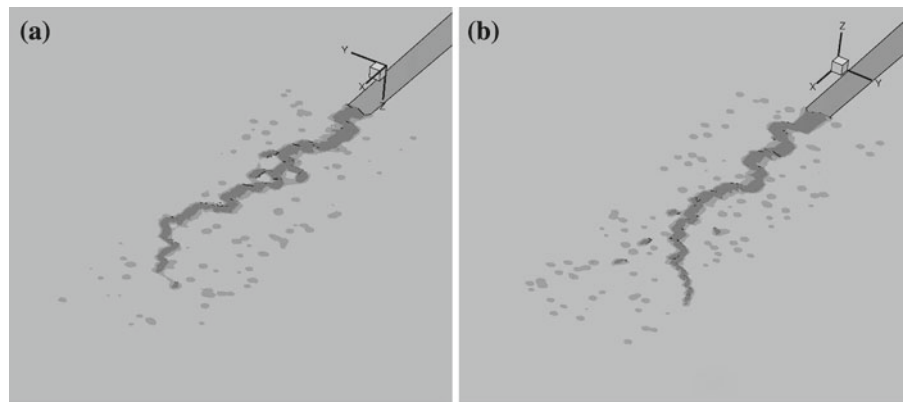

Fig. 2 Void volume fraction distribution showing the mode of crack growth for Material#2 ($\epsilon_N = 0.4$, $\sigma_N/\sigma_0 = 1.5$). **a** On $z = 0$. **b** On $z = h_z$. Note that the positive $y-$axis is in opposite directions in **a** and **b**

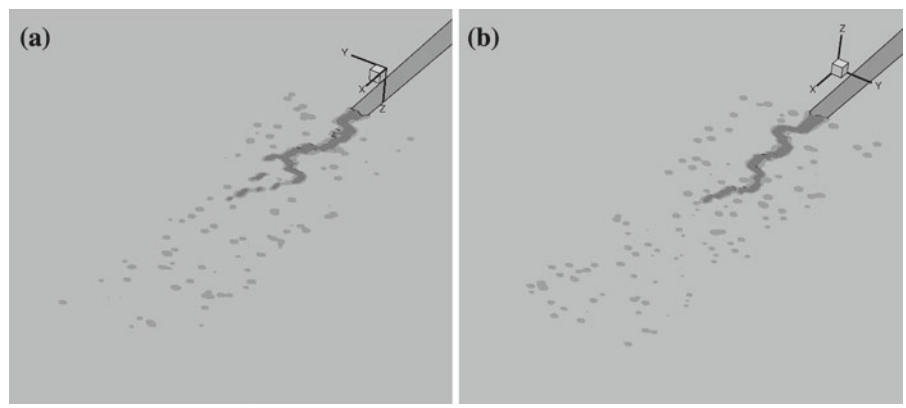

Fig. 3 Void volume fraction distribution showing the mode of crack growth for Material #2x ($\epsilon_N = 0.2$, $\sigma_N/\sigma_0 = 1.5$). **a** On $z = 0$. **b** On $z = h_z$. Note that the positive $y-$axis is in opposite directions in **a** and **b**

3 Results

3.1 Crack growth

Figures 2, 3 and 4 show distributions of void volume fraction f that indicate the crack growth path on the planes $z = 0$ and $z = h_z$ for Material #2, Material #2x and Material #3, respectively. In each case, the stage of loading corresponds to the last stage of loading computed for that case. Note that in (a) for all three figures the $y-$axis is positive to the left whereas in (b) for all three figures the $y-$axis is positive to the right. The dark gray regions show where $f \geq 0.1$ so that the material within those regions has essentially lost all stress

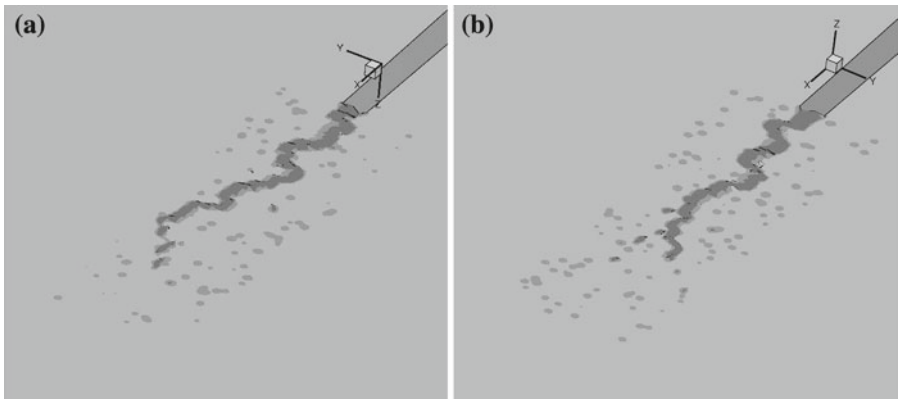

Fig. 4 Void volume fraction distribution showing the mode of crack growth for Material #3 ($\epsilon_N = 0.3$, $\sigma_N/\sigma_0 = 2.0$). **a** On $z = 0$. **b** On $z = h_z$. Note that the positive $y-$axis is in opposite directions in **a** and **b**

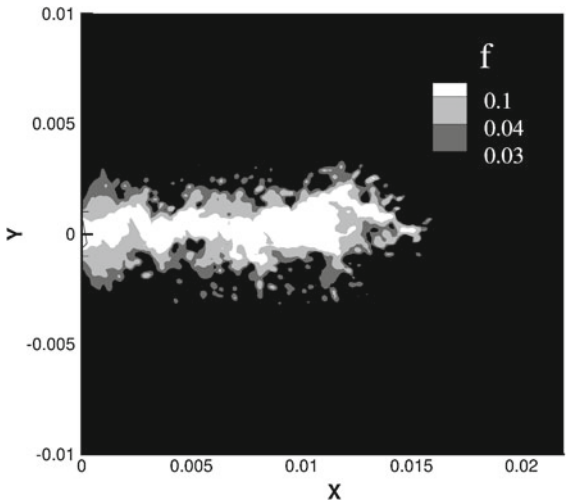

Fig. 5 Distributions of void volume fraction f in a plane $z =$ constant for material # 3 illustrating the definition of fracture surfaces based on void volume fraction threshold values of $f_t = 0.03,\ 0.04$ and 0.10

carrying capacity. The lighter gray regions which correspond to $0.1 \geq f \geq 0.01$ show the inclusions on the two planes that have nucleated voids. Shear localization can play a significant role in linking voids to the main crack. For Material #2x with $\epsilon_N = 0.2$, the calculation was terminated after a relatively small amount of crack growth because intense localized deformation led to the stable time step becoming very small.

3.2 Fracture surface definition

The first step in defining the fracture surface is to plot the void volume fraction f distribution on a cross section $z =$ constant. Next a threshold value f_t is chosen so that $f \geq f_t$ corresponds to a connected crack with f_t being the largest value that gives a connected crack over a predefined region. Figure 5 shows a typical cross section with contour values of $f = 0.03,\ 0.04$ and 0.10. The fracture surfaces for these three contour values are rather close. Changing the size of the cracked region modifies the value of f_t needed for a connected crack. Interestingly, the scaling behavior, and especially the value of the roughness exponent, was found to be largely independent of this value. On the contrary, the roughness amplitude was observed to slightly increase while the value of f_t was decreased.

For the fracture surfaces analyzed in the following, f_t is taken close to 0.10 but sufficiently small to avoid any uncracked ligaments behind the main crack. Regions with $f \geq f_t$, but that are not connected to the main crack, were found—these are not shown in Fig. 5. They do not contribute to the roughness of the fracture surfaces.

The roughness is computed for the two fracture surfaces produced by each calculation. One fracture surface, termed as the lower fracture surface, is obtained from the smallest value of z, for a given position (x, y) in the mean fracture plane, for which $f \geq f_t$ on the connected crack while the other fracture surface, termed the upper fracture surface, corresponds to the largest value of z, for a given position (x, y) in the mean fracture plane, for which $f \geq f_t$ on the connected crack. The crack profiles obtained from the lower and upper fracture surfaces are denoted by $h^{\text{bot}}(x)$ and $h^{\text{top}}(x)$, respectively. These are shown on Fig. 6 for the void volume fraction distribution of Fig. 5. The jumps in the profiles reflect the overhangs in the connected crack

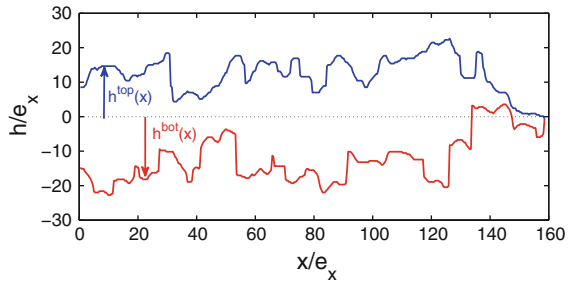

Fig. 6 Fracture profiles extracted along the crack propagation direction x obtained from the void volume fraction distribution of Fig. 5 using $f_t = 0.04$ for material # 3

as seen in the porosity distribution. Our definition of the crack profiles mimics a profilometer that measures only the highest point on the fracture surface and so prevents the presence of overhang on the crack surfaces analyzed subsequently.

4 Statistical analysis of fracture surfaces

4.1 Correlation functions of fracture surfaces and roughness exponent

We first characterize the fluctuations of heights of the fracture surface using the correlation function, Δh, defined as

$$\Delta h(\delta x) = \sqrt{\langle [h(x+\delta x,\ y) - h(x,\ y)]^2 \rangle_{x,\,y}} \qquad (17)$$

Here, $\langle\ \rangle_x$ denotes the average over x and y. The quantity $\Delta h(\delta x)$ can be interpreted as the typical difference of height between two points separated by a distance δx along the mean fracture plane. We focus on the correlation of heights in the direction of propagation only (x-axis), the width of the specimen in the perpendicular direction z being too small to allow a statistical analysis of the roughness in that direction.

The correlation function is computed for both the upper and lower fracture surfaces. The final correlation function is then obtained by averaging over these statistically equivalent surfaces. Indeed, from symmetry arguments, we expect the upper and lower fracture surfaces in each calculation to share similar statistical properties. The correlation function $\Delta h(\delta x)$ is shown in Fig. 7 on a logarithmic scale, after normalization of the axis by the element spacing e_x along the x-axis in the fine mesh region. Figure 7a shows plots for the four inclusion distributions analyzed in Needleman et al. (2012) corresponding to material #1 ($\epsilon_N = 0.3$ and $\sigma_N/\sigma_0 = 1.5$) using the same notation as in Needleman et al. (2012) to identify the inclusion distributions. The correlation functions exhibit a power law behavior

$$\Delta h(\delta x) \propto \delta x^{\beta} \qquad (18)$$

over more than two decades, characterized by the roughness exponent β. In this logarithmic representation, β is the slope of the solid straight lines, power law fits of the correlation functions computed from the fracture surfaces. Although the roughness amplitude—the position of the lines along the ordinates—may vary from one sample to another, the slope remains rather independent of the inclusion spatial distribution, as illustrated by the values of β given in the legend of the figure and obtained from a power law fit of these curves. These results give an average roughness exponent $\beta = 0.55 \pm 0.02$, independent of the inclusion distribution.

Our calculations capture the self-affine nature of ductile fracture surfaces, as observed experimentally in Bonamy and Bouchaud (2011), and as also found numerically in Needleman et al. (2012), but here over a larger range of length scales than in Needleman et al. (2012). Since quadratic elements are used the mesh spacing is $e_x/2$ but the scaling in Fig. 7 holds for even smaller δx values. This indicates that the interpolation procedure between mesh points when defining the fracture surface geometry still preserves the roughness scaling. In Needleman et al. (2012) values $0.4 < \beta < 0.6$ were reported for the simulations in Fig. 7a. The procedure used in this study to define the fracture surfaces from the porosity field gives a more precise characterization of the crack roughness, a more uniform value of the roughness exponent and the value of the roughness exponent β exhibits a smaller variation with the inclusion distribution than in Needleman et al. (2012). There are variations in the amplitude of the roughness that reflect variations in the threshold value f_t of the porosity used to define the fracture surfaces. Nevertheless, despite these fluctuations, the value of the roughness exponent is very robust, and changes very weakly from one inclusion distribution to another. We have also checked that the value of the roughness exponent does not depend much on the value of the threshold f_t used to define the fracture surfaces using both $f_t = 0.04$ and $f_t = 0.10$, supporting the value $\beta \simeq 0.55$ reported in this study.

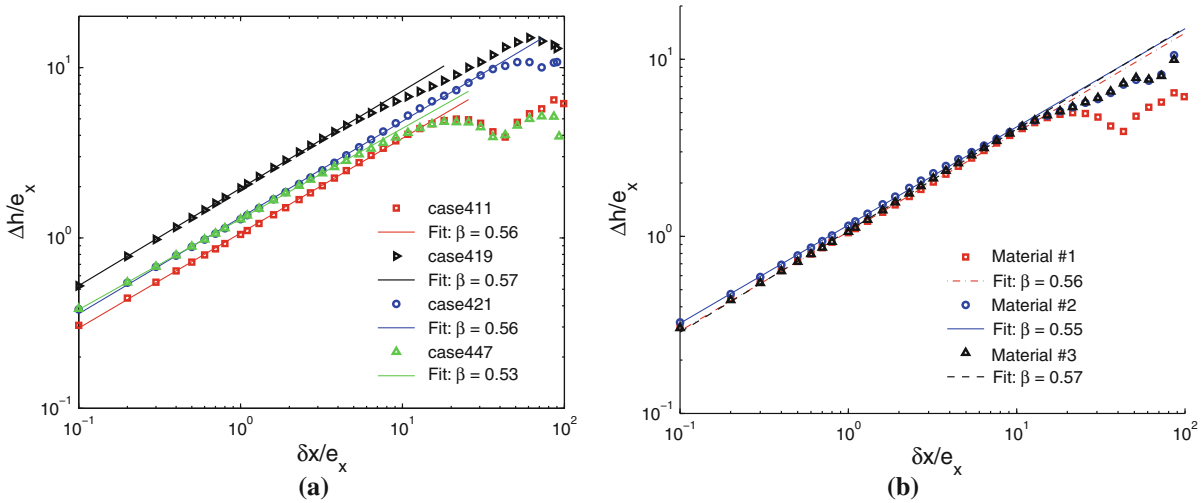

Fig. 7 Correlation function of the roughness of simulated fracture surfaces. **a** Material # 1: scaling behavior of the crack roughness observed for four different spatial distributions of the inclusions (see Needleman et al. 2012) characterized by a similar roughness exponents $\beta = 0.55 \pm 0.02$. **b** Comparisons of materials #1, #2 and #3: Scaling behavior of the crack roughness for the same spatial distribution of inclusions, but with different material properties. regardless of the value of the nucleation threshold, the roughness follows power law behavior with a roughness exponent $\beta = 0.56 \pm 0.01$

Figure 7b shows the effect of varying a material parameter for a fixed spatial distribution of inclusions. The inclusion distribution chosen here is case411 (Needleman et al. 2012). In one calculation, the void nucleation strain is taken to be $\epsilon_N = 0.4$ (material #2) while in the other calculation $\sigma_N/\sigma_0 = 2.0$ (material #3). All other material and void nucleation parameters remain fixed. Also, for comparison purposes, the data for case411 with the reference void nucleation parameters (material # 1) is also plotted. The simulated fracture surfaces here show a power law behavior, with a roughness exponent, $\beta \simeq 0.56$, rather independent of the material properties in the range investigated. This result is consistent with a large body of experimental work that reports a universal value of the roughness exponent, independent to a large extent of the microstructure of the material studied, its mechanical properties or the loading conditions used during the fracture test as seen in Bonamy and Bouchaud (2011), Bouchaud et al. (1990), Ponson et al. (2006).

4.2 Non-Gaussian statistics of height fluctuations

As seen in Fig. 7, the Hurst exponents calculated for the various inclusion distributions and material parameter variations considered here and in Needleman et al. (2012) are nearly the same. In Vernède et al. (2013) the full statistics of fracture surface height fluctuations were obtained for cracks in a variety of materials. It was found that the height fluctuations could be described by a distribution that differed from a Gaussian by having power law tails. The deviation from Gaussian statistics was found to be material dependent. Therefore, in order to explore possible effects of material characteristics on the predicted fracture surface morphology, we investigate the full statistics of height variations $\delta h(x, y)$ defined by

$$\delta h(x, y) = h(x + \delta x, y) - h(x, y) \tag{19}$$

Following Ponson (2007), Santucci et al. (2007), the procedure used to compute the histogram $P(\delta h)$ at a given scale δx is the following.

1. We fix first a value of δx.
2. For each location (x, y) on both the upper and lower fracture surface, the corresponding height variations δh are computed. This procedure results in a large set $\{\delta h\}_{\delta x}$ of height variations at a given scale δx.
3. The histogram of this set of values is computed. The histogram of δh is calculated by placing into 'boxes' $[b_{\min} b_2]$, $[b_2 b_3]$,..., $[b_{n-1} b_{\max}]$ the values of δh where the side b_1, b_2 of the boxes are distrib-

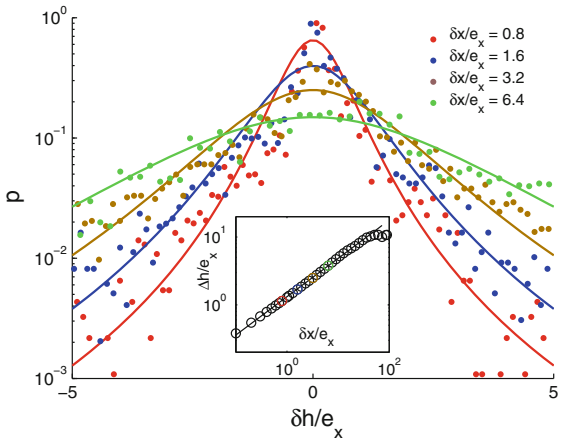

Fig. 8 Histograms $P(\delta h|\delta x)$ of height variations δh (see Eq. (19)) for various values of δx for material #1 and the spatial distribution of particles labeled case421 in Needleman et al. (2012). The *solid lines* are fits based on the Student's distribution of Eq. (20) using various values of the parameters k and δh_c.The *inset* represents the correlation function of the surface. The *points* (or second moment) corresponding to the distributions represented in the main panel are plotted using the same color code

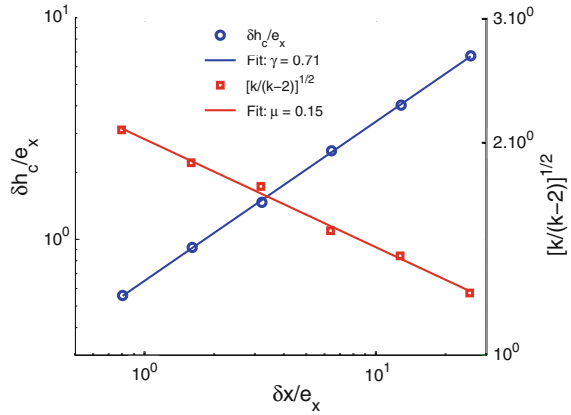

Fig. 9 Variations of the parameters $\sqrt{k/(k-2)}$ and $\delta h_c/e_x$ obtained from the fit of the roughness distributions $P(\delta h)$ shown in Fig. 8 for case 421 in Needleman et al. (2012) using Student's distribution (see Eq. (20)). The transition from power law tails ($\sqrt{k/(k-2)} \gg 1$) to Gaussian ($\sqrt{k/(k-2)} \simeq 1$) statistics as the length scale δx increases is characterized by the exponent $\mu = 0.15$. The typical value of δh_c of the roughness extracted using fits by Student's distribution also evolves as a power law of the length scale δx with exponent $\gamma = 0.71$

uted homogeneously between $b_{\min} = \min[\delta h]$ and $b_{\max} = \max[\delta h]$.

4. The histogram or probability density

$$P_i\left(\delta h_i = \frac{b_i + b_{i+1}}{2}|\delta x\right)$$

is calculated as the fraction of values of δh contained in the i^{th} box.

In order to study the scaling behavior of the fracture surface roughness, this procedure is repeated for various scales δx, leading to a family of histograms $P(\delta h|\delta x)$. An important property is that the standard deviation of the distributions $P(\delta h|\delta x)$ corresponds to the correlation function $\Delta h(\delta x)$ of the fracture surfaces, as can be observed from its definition in Eq. (17).

The distribution $P(\delta h|\delta x)$ is shown in Fig. 8 for four values of δx for the simulation labeled case421 in Needleman et al. (2012). The larger the value of δx, the broader the distribution, as expected from the scaling of the correlation function $\Delta h(\delta x) \propto \delta x^{\beta}$. The standard deviation of these histograms is plotted in the inset as a function of δx using the same color code as in the main panel. As expected, the standard deviation evolves as a power law with exponent $\beta = 0.56$, in agreement with the plot of $\Delta h(\delta x)$ shown in Fig. 7.

The distribution of height variations computed on numerical fracture surfaces are not Gaussian, but exhibit fat tails with power law behavior $P(\delta h) \propto \delta h^{(k+1)/2}$ for large values of δh. This means that large height fluctuations are not exponentially rare on ductile fracture surfaces as is the case for brittle fracture surfaces (Ponson et al. 2007). Indeed, the crack profiles in the calculations here display a non-negligible number of abnormally large fluctuations δh, as qualitatively seen in Fig. 6.

To describe this effect more quantitatively, the distributions $P(\delta h)$ are described using a family of probability distributions referred to as Student's t distributions

$$t_{k,\delta h_c}(\delta h) \propto \frac{1}{\delta h_c}\left(1 + \frac{1}{k}\left(\frac{\delta h}{\delta h_c}\right)^2\right)^{-(k+1)/2} \tag{20}$$

with parameters k and δh_c, and represented by solid lines in Fig. 8. For reasons discussed in the next section, it is more appropriate to consider the parameter $\sqrt{k/(k-2)}$ instead of k.

These parameters, obtained from the fit of the distributions $P(\delta h|\delta x)$, are represented in Fig. 9 as a function of the scale δx. The first parameter that characterizes the shape of the distribution decreases as a power law with the scale δx

$$\sqrt{\frac{k}{k-2}} \propto \delta x^{-\mu} \tag{21}$$

with $\mu = 0.15$ as illustrated by the straight line variations in the logarithmic representation of Fig. 9.

The second fitting parameter used to describe the roughness distributions $P(\delta h|\delta x)$ is also represented in Fig. 9 as a function of the scale δx. It here increases as a power law

$$\delta h_c \propto \delta x^{\gamma} \tag{22}$$

with exponent $\gamma = 0.71$.

The ductile crack profiles studied here exhibit a more complex behavior than brittle fracture surfaces. Indeed, in brittle materials, distributions of height variations follow a Gaussian behavior at all scales (Ponson 2007; Ponson et al. 2007). In our description based on Student's t distribution, this corresponds to $k \to \infty$, or equivalently, to $\sqrt{k/(k-2)} = 1$, for any value of δx. In other words, only one exponent is needed to describe the scaling of the roughness distribution, since $\mu = 0$. For ductile fracture surfaces, not one, but three scaling exponents β, μ and γ are required. However, this can be reduced to two independent exponents based on a simple relationship. Using the definition (20) of Student's t distribution, one can show that its second moment, and so the correlation function, varies as

$$\Delta h(\delta x) \propto \delta h_c \sqrt{k/(k-2)} \tag{23}$$

As a result, from the scaling relations in Eqs. (18), (21) and (22), one obtains

$$\beta = \gamma - \mu. \tag{24}$$

This relation is satisfied by the exponents extracted here for which $\beta = 0.56$ (case421) was measured (see Fig. 7). This supports our description of the roughness statistics based on Student's t distribution.

The relation between exponents suggests an interpretation of the roughness exponent β that characterizes the scaling behavior of the correlation function with the scale δx as the combined effect of the variations of the typical roughness δh_c with the scale δx and the variations in the actual shape of the distribution of height fluctuations. It also suggests that the universal value of the roughness exponent β relies on the value of μ that describes the change in the shape of roughness distribution. Experimental results in Vernède et al. (2013) are consistent with these findings: the statistical analysis of both aluminum alloy and mortar fracture surfaces indicates a similar behavior, with a measured value $\mu^{\text{exp}} \simeq 0.15$. However, the experimental value of the second exponent, $\gamma^{\text{exp}} \simeq 0.9$, is larger than the value obtained for the calculated fracture surfaces here.

In the following, we use the above analysis of the distribution of height variations to compare the fracture surfaces obtained for materials #1, #2 and #3.

4.3 Roughness statistics: comparison between the materials

The analysis in Sect. 4.2 revealed that the scaling of the roughness distribution of ductile fracture surfaces could be described using Student's $t_{k,\delta h_c}$ distribution introduced in Eq. (20), with the adjustable parameters $\sqrt{k/(k-2)}$ and δh_c that follow power laws with the scale δx. We focus in this section on the parameter $\sqrt{k(k-2)}$ that characterizes the distribution shape. For a finite value of the parameter k, Student's t distribution displays fat tails with

$$t_{k,\delta h_c}(\delta h) \propto \delta h^{(k+1)/2} \quad \text{for } \delta h \gg \delta h_c$$

while $t_{k,\delta h_c}(\delta h)$ approaches a Gaussian distribution when k tends to infinity. As a result, this family of distributions is suited to describe a transition from power law tails to Gaussian statistics. In particular $\sqrt{k/(k-2)} = 1$ for a Gaussian distribution and $\sqrt{k/(k-2)} > 1$ otherwise. We expect the value of $\sqrt{k/(k-2)}$ to indicate the distance from Gaussian behavior.

The analysis of the fracture surface of material #1 has revealed that $\sqrt{k/(k-2)}$ remains larger than one, indicating fat tails statistics and deviation from a Gaussian distribution at the length scales investigated (see Fig. 9). However, extrapolating the power law behavior $\sqrt{k/(k-2)} \sim \delta x^{-\mu}$ towards larger values of δx, predicts that it will reach $\sqrt{k/(k-2)}(\delta x = \xi) = 1$ at the crossover length $\delta x = \xi$. Interestingly, it means that for $\delta x > \xi$, the fracture surface might recover Gaussian statistics. Such an extrapolation leads to $\xi = 100 e_x$ for material #1.

The transition from fat tail statistics for $\delta x < \xi$ to Gaussian behavior for $\delta x > \xi$ calls for an interpretation in terms of fracture mechanisms. In the scenario proposed in Vernède et al. (2013), Gaussian statistics of the roughness would be reminiscent of brittle fracture surfaces while distributions with fat tails would be signature of damage mechanisms. This behavior is fairly consistent with the scaling behavior of the correlation function that gives roughness exponents of the order of $\beta = 0.5$ for brittle failure and larger values around $\beta = 0.6$ at a smaller scale when failure is accompanied by damage mechanisms (Bonamy

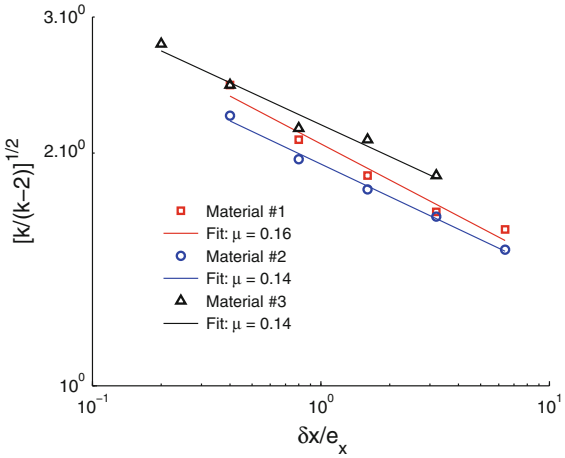

Fig. 10 Variations of the parameter $\sqrt{k/(k-2)}$ used in the fit by Student's distribution, Eq. (20), of the histograms $P(\delta h)$ of height fluctuations as a function of δx

et al. 2006; Morel et al. 2008). The crossover length between the two regimes - large exponents and fat tail statistics at small scale to small exponents with Gaussian statistics at large scale - may be a reflection of the size scale associated with the micro mechanism of fracture. If so, the value of ξ extracted from the analysis of the roughness statistics could serve as a length scale associated with the underlying damage process.

Figure 10 compares the variations of the parameter $\sqrt{k/(k-2)}$ for the materials analyzed. The power law decay differs from one material to another. The exponent $\mu \simeq 0.15$ —the slope of the straight line variations in this logarithmic representation—remains rather constant. But the variations in the position along the ordinates indicate different values of ξ, and more generally, different level of deviations from Gaussian (and so brittle) behavior.

The deviation from Gaussian behavior is more pronounced for material #3 than for material #2 for which the values of $\sqrt{k/(k-2)}$ is smaller at all length scales δx. This may indicate that material #3 is more ductile than material #2 which is expected due to the larger value of the nucleation stress for the large inclusions. Extrapolation of $\sqrt{k/(k-2)}$ to large values of δx indicates that the crossover value $\xi = 300e_x$ for material #3 which is much larger than the value estimated for the materials #1 and #2.

The comparison of material #1 with material #2 is more complex. The relative position of the curves $\sqrt{k/(k-2)}$ indicates stronger deviations from Gaussian behavior for material #1. However, the extrapolated value of $\xi \simeq 100e_x$ gives a similar value for both materials.

5 Discussion

Calculations have been carried out for a fixed size, density and distribution of discretely modeled void nucleating inclusions. The statistics of the fracture surfaces was investigated. In addition, the statistics of the fracture surfaces obtained in Needleman et al. (2012) were recalculated. In Needleman et al. (2012), the fracture surface was defined by a threshold value $f_t = 0.1$, somewhat smaller than the material parameter f_t used in the constitutive model to define final failure. In the present studies, in some cases, an even smaller value, $f_t = 0.03$, is chosen to define a well connected crack surface. Fig. 5 shows that the crack surfaces obtained by these definitions are rather close, as the value of f increases steeply in the material near the fully open crack. In Needleman et al. (2012), a thickness average of the fracture surface height was calculated and this average profile was used to obtain the correlation function $\Delta h(\delta x)$. Here, instead, $\Delta h(\delta x)$ is calculated for each cross section, and is subsequently averaged, and it turns out that this procedure gives power law scaling over a larger range, with less difference between the various inclusion distributions in Needleman et al. (2012). Also in Needleman et al. (2012) only the roughness exponent was calculated whereas here we calculate more complete fracture surface statistics.

As noted in Needleman et al. (2012) the calculations contain several length scales: (1) the mean spacing between inclusion centers; (2) the inclusion radius; (3) the slice thickness; and (4) the finite element mesh spacing. A significant difference between these length scales is that the first three are physically relevant length scales whereas any dependence of the results on the finite element mesh length scale is a numerical artifact. Whether or not there is a significant effect of the finite element mesh spacing on the predicted statistics of fracture roughness remains to be determined.

Our results give rise to a value of $\beta = 0.56 \pm 0.03$ that is essentially independent of the inclusion distributions and fracture properties considered and that is also close to the value $\beta^{3D} \simeq 0.6$ reported for 3D fracture surfaces of a wide range of ductile and quasi-brittle

materials in the crack propagation direction Ponson et al. (2006), Ponson et al. (2006). While the probability distribution of heights is a Gaussian for brittle fracture, it is more complex for ductile fracture surfaces. We showed that Student's t distribution can fit all the histograms in Fig. 8. This distribution is equivalent to a Gaussian at sufficiently small values of $\delta h/e_x$ but crosses over to a power-law at larger values. Also, as seen in Fig. 8 for small values of $\delta x/e_x$ the computed distributions display fat power law tails whereas for sufficiently large values of $\delta x/e_x$ the distribution is well-fit by a Gaussian. The transition from fat tail to Gaussian statistics is described by introducing a second exponent $\mu \simeq 0.15$. In the experiments in Vernède et al. (2013) where the roughness statistics were calculated as an average over all directions in the fracture surface, the statistics were also observed to deviate from a Gaussian and the deviation was well-described by two exponents. The value of μ was close to the one obtained here but the value of γ was larger than in our calculations. Hence, while for brittle fracture surfaces, knowledge of the roughness index β is sufficient to describe completely the probability distribution, for ductile fracture surfaces independent exponents are needed.

Our results indicate that for ductile fracture surfaces there is a length characterizing the crossover from power law to Gaussian statistics. The results also suggest that this length may correlate with the size of the fracture process zone. What remains to be determined is the extent to which this crossover length as well as other aspects of the non-Gaussian statistics correlate with measures of fracture toughness such as K_{Ic} and crack growth resistance curves. For the type of materials considered here, this requires more extensive calculations with increased crack growth, larger variations of inclusion density and distribution, and greater variation in material properties. Such calculations are being undertaken and the results here suggest the possibility of a connection being made between post-mortem fracture surface statistics and crack growth resistance.

6 Conclusions

1. A central result of this paper is that, for the material parameter variations analyzed, the computed ductile fracture surfaces exhibit self-affine properties with similar values of the fracture surface roughness exponent β but their full statistical properties differ.
2. For the ductile fracture surfaces analyzed:

- The computed fracture surfaces are self-affine over a range of length scales of about two orders of magnitude.
- The computed values of the fracture surface roughness exponents along the crack growth direction are not sensitive to the larger particle distributions nor to the fracture parameter variations investigated.
- The computed fracture surface roughness distributions are not Gaussian but they are all well fitted by Student's distribution. Both the roughness exponent $\beta = 0.56 \pm 0.03$ and the exponent $\mu \simeq 0.15$ characterizing the transition with $\delta x/e_x$ from fat tail to Gaussian statistics are found to be rather independent of the spatial distributions of the larger inclusions and of material parameters in the range investigated.
- The computed full fracture surface roughness statistics vary with the fracture parameters investigated.

Acknowledgments The financial support provided by the U.S. National Science Foundation through Grant CMMI-1200203 and by the European Union through the ToughBridge Marie Curie Grant (LP) is gratefully acknowledged. We also thank Jean-Philippe Bouchaud and Stéphane Vernède for fruitful discussions

References

Alava MJ, Nukala PKVV, Zapperi S (2006) Statistical models of fracture. Adv Phys 55:349–476

Belytschko T, Chiapetta RL, Bartel HD (1976) Efficient large scale non-linear transient analysis by finite elements. Int J Numer Methods Eng 10:579–596

Bonamy D, Ponson L, Prades S, Bouchaud E, Guillot C (2006) Scaling exponents for fracture surfaces in homogeneous glass and glassy ceramics. Phys Rev Lett 97:135504

Bonamy D, Bouchaud E (2011) Failure of heterogeneous materials: a dynamic phase transition? Phys Rep 498:1–44

Bouchaud E, Lapasset G, Planès J (1990) Fractal dimension of fractured surfaces: a universal value? Europhys Lett 13:73–79

Bouchaud E (2003) The morphology of fracture surfaces: a tool for understanding crack propagation in complex materials. Surf Rev Lett 10:797–814

Bouchbinder E, Mathiesen J, Procaccia I (2004) Roughening of fracture surfaces: the role of plastic deformation. Phys Rev Lett 92:245505

Cherepanov GP, Balankin AS, Ivanova VS (1995) Fractal fracture mechanics–a review. Eng Fract Mech 51:997–1033

Chu CC, Needleman A (1980) Void nucleation effects in biaxially stretched sheets. J Eng Mater Technol 102:249–256

Gurson AL (1975) Plastic flow and fracture behavior of ductile materials incorporating void nucleation, growth and interaction. Ph.D. Thesis, Brown University.

Måløy KJ, Hansen A, Hinrichsen EL, Roux S (1992) Experimental measurements of the roughness of brittle cracks. Phys Rev Lett 68:213–215

Mandelbrot BB, Passoja DE, Paullay AJ (1984) Fractal character of fracture surfaces of metals. Nature 308:721–722

Morel S, Bonamy D, Ponson L, Bouchaud E (2008) Transient damage spreading and anomalous scaling in mortar crack surfaces. Phys Rev E 78:016112

Nakano A, Kalia RK, Vashista P (1995) Dynamics and morphology of brittle cracks: a molecular-dynamics study of silicon nitride. Phys Rev Lett 75:3138–3141

Needleman A, Tvergaard V, Bouchaud E (2012) Prediction of ductile fracture surface roughness scaling. J Appl Mech 79:031015

Peirce D, Shih CF, Needleman A (1984) A tangent modulus method for rate dependent solids. Comput Struct 18:875–887

Ponson L, Auradou H, Vié P, Hulin JP (2006) Low self-affine exponents of fractured glass ceramics surfaces. Phys Rev Lett 97:125501

Ponson L, Bonamy D, Bouchaud E (2006) Two dimensional scaling properties of experimental fracture surfaces. Phys Rev Lett 96:035506

Ponson L, Bonamy D, Auradou H, Mourot G, Morel S, Bouchaud E, Guillot C, Hulin J-P (2006) Anisotropic self-affine properties of experimental fracture surfaces. Int Fract 140:27–36

Ponson L (2007) Crack propagation in disordered materials: how to decipher fracture surfaces. Ann Phys 32:1–120

Ponson L, Auradou H, Pessel M, Lazarus V, Hulin J-P (2007) Failure mechanisms and surface roughness statistics of fractured Fontainebleau sandstone. Phys Rev E 76:036108

Ramanathan S, Ertas D, Fisher DS (1997) Quasistatic crack propagation in heterogeneous media. Phys Rev Lett 79:873–876

Santucci S, Måløy KJ, Delaplace A, Mathiesen J, Hansen A, Bakke J, Schmittbuhl J, Vanel L, Ray P (2007) Statistics of fracture surfaces. Phys Rev E 75:016104

Tvergaard V (1981) Influence of voids on shear band instabilities under plane strain conditions. Int J Fract 17:389–407

Tvergaard V (1982a) On localization in ductile materials containing spherical voids. Int J Fract 18:237–252

Tvergaard V (1982b) Influence of void nucleation on ductile shear fracture at a free surface. J Mech Phys Solids 30:399–425

Tvergaard V, Needleman A (1984) Analysis of the cup-cone fracture in a round tensile bar. Acta Metall 32:157–169

Vernède S, Cao Y, Bouchaud JP, Ponson L (2013) Extreme events and non-Gaussian statistics of experimental fracture surfaces (submitted for publication)